IEEE Access
Multidisciplinary | Rapid Review | Open Access Journal

Received July 22, 2019, accepted July 25, 2019, date of publication July 29, 2019, date of current version August 13, 2019.

Digital Object Identifier 10.1109/ACCESS.2019.2931646

Enhanced Attitude Control of Unmanned Aerial Vehicles Based on Virtual Angular Accelerometer

ZIJUN REN[1,2], (Student Member, IEEE), WENXING FU[2], YONGZE LI[3], BINBIN YAN[1,2], SUPENG ZHU[1], AND JIE YAN[1,2]

[1]School of Astronautics, Northwestern Polytechnical University, Xi'an 710072, China
[2]Unmanned System Research Institute, Northwestern Polytechnical University, Xi'an 710072, China
[3]Institute of Systems Engineering, China Academy of Engineering Physics, Mianyang 621000, China

Corresponding author: Supeng Zhu (supengzh@nwpu.edu.cn)

This work was supported by the NSFC-NSAF under Grant U1630127 and Grant U1730135.

ABSTRACT The small unmanned aerial vehicles are susceptible to wind disturbances due to the turbulent environment at their low operational altitude. Compared to conventional IMU output, the phase-advanced information provided by angular acceleration measurement is more beneficial for flight stability. This paper presents a general and systematic approach to enhance the attitude stability of small fixed-wing unmanned aerial vehicles. The methodology begins by designing a virtual angular accelerometer (VAA), which is based on 4 MEMS IMUs measurement fusion. Then, the angular acceleration is exploited to estimate and compensate disturbances. Finally, an enhanced attitude control scheme is developed to improve attitude tracking performance, where linear or nonlinear control approaches can be adopted. A VAA-based backstepping controller (BS) is designed and its stability is analyzed via Lyapunov function. Three simulation cases are carried out to verify the performance of tracking accuracy, robustness, and disturbance rejection. PID and backstepping methods are applied to the scheme. As a comparison, a widely used nonlinear disturbance observer (NDO)-based robust controller (RC) is studied. The simulation results show the excellent performance of the sensor-based VAA to observe the fast time-varying disturbance, where the NDO causes the time delay and phase lag. The tracking accuracy of the enhanced controllers (PID+VAA, BS+VAA, and RC+VAA), compared to the basic controllers, are improved by 14.3%–93.7% and the closed-loop control systems gain notable robustness.

INDEX TERMS Small UAV, attitude control, multi-IMUs, EKF, angular acceleration.

I. INTRODUCTION

The rapid development of Unmanned Aerial Vehicles (UAVs) has attracted public attention in recent years. The PwC estimates the UAV powered market value at over 127 billion$ [1]. The characteristics of UAV, such as low cost, easy accessibility, none pilot casualty and high efficiency, motivate various applications in both civil and military scenarios [2]. Researchers all over the world have been exploring the possibilities of UAVs for decades, particularly of the small ones. Promising applications have arisen in the fields of infrastructure [3], [4], agriculture [5], air quality monitoring [6], transport [8], fighting fires [9] and battlefield reconnaissance [10]. Such applications pose new challenges to flight control system due to the increasingly complex operation environment.

UAVs equipped with optical payload sensors are especially suitable for intelligence, surveillance, and reconnaissance (ISR) missions, which require a high level of stability for the sensors to focus on targets. The work of Merritt [11] has shown that the angular vibration of the UAV is usually the largest contributor of the disturbances that affect the optical sensor performance. Large UAVs utilize high-performance inertial platforms to isolate the external disturbances, whereas small UAVs usually have the cameras installed on the airframe directly or low-cost gimbals. For small filming UAVs, disturbances can easily cause defocus and blur in images or even lose targets, which is very likely to result in failure in recognizing and tracking targets. Therefore, for a small UAV, a high degree of angular stability is essential for its ISR-mission quality.

The associate editor coordinating the review of this manuscript and approving it for publication was Zhen Li.

Small UAVs typically fly within the ABL (atmospheric boundary layer: extends up to 5 km above ground). The wind condition here is complicated and changeable, especially in urban area, where turbulence intensities reach 40% within tens of meters above the ground [12] and wind speeds reach 60% of the desired airspeed [14]. The local AOA, across the wing span for a small UAV flying in turbulence near ground, may vary in the order of $\pm 10^{\circ}$ [15]. In windy or turbulent environment, wind perturbations can easily degrade the performance of optical system. Workdays of missions, such as search, rescue and inspection, may be reduced and costs may be increased because of bad weather. Wind disturbance rejection is important for small UAVs to accomplish these tasks.

Mohamed *et al.* [12], [16] assert that it is better to detect disturbances relatively quickly, especially before the UAV starts to respond. The commercial gyroscopes require the small UAV to respond inertially to detect a motion perturbation. Angular acceleration measurements provide phase-advanced information that conventional IMU cannot. It must take unusual steps to measure angular acceleration of a small UAV.

Recently, significant progress has been made on the disturbance rejection control of small rotor UAVs [19], [32]–[35]. In [34], a linear extended state observer (LESO) was designed to estimate the unknown disturbance. And the disturbance was compensated to ensure the robustness of the control strategy. To guarantee the closed loop control system converged in finite time, a disturbance observer with finite time convergence (FTDO) was designed to actively online estimate the unknown uncertainties and disturbances [35]. Extended state observers for inner and outer loop were designed to estimate unmeasured states and lumped disturbances [32]. In [19], [33], high-order extended state observers were explored to estimate the uncertainties and full-states of quadrotors. These model-based observers were usually built on the estimation that the derivative of disturbance $\dot{\boldsymbol{d}} \approx 0$ or $\|\dot{\boldsymbol{d}}\| \leq C$ to reach a exponential stability or boundedness. These ESO or DO based control methods showed excellent performance when the UAVs encountered slow-varying disturbances. However, there appears performance degradation of the model-based observers when estimating high frequency disturbances, referring to Fig. 5.

In circular motion, there exists a simple relationship between angular acceleration and linear acceleration

$$\boldsymbol{a}_t = \boldsymbol{\alpha} \times \boldsymbol{\rho}, \tag{1}$$

where, $\boldsymbol{a}_t$ and $\boldsymbol{\alpha}$ are the tangential acceleration and angular acceleration respectively of a point rotating around a fixed center and $\boldsymbol{\rho}$ represents the off-center vector. Accelerometers, of course, could be exploited to estimate the angular acceleration. Luckily, MEMS IMUs are cheap and off the shelf. Schopp *et al.* study the gyroscope-free inertial measurement unit (GF-IMU) composed of only linear accelerometers [17]. The GF-IMU measured the linear acceleration directly and the angular acceleration indirectly via (1). Two valid accelerometers configurations were tested, both containing 4×3 sensors. In [18], a distributed accelerometers array of different sensor numbers ranging from 14 to 36 was tested, arriving at an empirical formula for estimation error $\sigma_e = 0.022 + \frac{1}{(n-11)^2}$, where $n \geq 12$ is the sensor number. Least square algorithm was used to estimate the 12 state variables including angular acceleration.

The existing disturbance rejection control methods show good qualities in compensating slowly-varying disturbances. However, in situations of high-frequency disturbance (air-dropping cargo, flying robotic arm) or high-precision attitude control (aerial photography), the model-based observers cause delay and phase lag. In this paper, we take advantage of the high response frequency of MEMS IMU to design a virtual angular accelerometer to observe disturbance and develop an enhanced attitude control scheme. Our contributions are listed below:

1) We propose a novel method to measure angular acceleration based on multi-IMUs information fusion, which is used to estimate the disturbances. Unlike conventional model-based observers, the sensor-based observer has a very fast response time in <10 ms, which is suitable for high-frequency disturbance and high-precision attitude control. And the fusion results also provide better measurements of inertial states.
2) Based on the sensor-based virtual angular accelerometer, we design an enhanced attitude control structure to improve the flight performance.
3) The enhanced control scheme shows remarkable improvement and robustness against uncertainties and disturbances.

The rest of the paper is organized as follows. The Small UAV used here is described in Section II. Section III presents the virtual angular accelerometer. The enhanced attitude control strategy and the abundant simulations are presented in Section IV and Section V respectively. Conclusions and future work are described in Section VI.

II. SMALL FIXED-WING UAV DYNAMICS

The Ultra Stick 25e (US 25e) aircraft chosen for the research is a commercially available small RC model airplane with a conventional configuration, which has a main wing, a vertical tail and a horizontal tail with aileron, rudder and elevator respectively, as shown in Fig. 1. The aircraft is assumed as symmetric rigid body with moving components, such as the rotor and the control surfaces. $\mathcal{B} \equiv O_b X_b Y_b Z_b$ and $\mathcal{I} \equiv O_i X_i Y_i Z_i$ are the body coordinate system and the inertial coordinate system respectively. For small UAVs, $\mathcal{I}$ usually refers to the local flat earth reference frame. O_b is the center of mass of the airplane.

The airplane orientation is described by the three Eulerian angles $\boldsymbol{\xi} = [\phi, \theta, \psi]^T$. T denotes matrix transpose. The nonlinear attitude model of the aircraft is expressed using

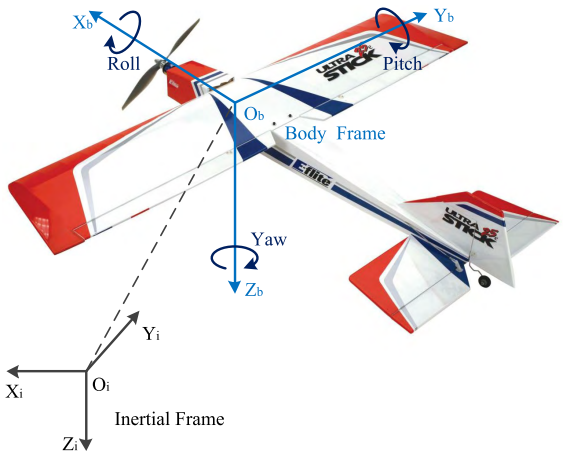

FIGURE 1. The US 25e RC airplane.

TABLE 1. US 25e mass and geometry characteristics.

Gross mass, m	1.9 kg
Wingspan, b	1.27 m
Wing area, S	0.31 m^2
Mean aerodynamic chord, $\bar{c}$	0.25 m
Roll moment of inertia I_x	0.089 kg·m^2
Pitch moment of inertia I_y	0.14 kg·m^2
Yaw moment of inertia I_z	0.16 kg·m^2
Moment of inertia I_{xz}	0.014 kg·m^2
Moment of inertia I_{xy}, I_{yz}	≈0 kg·m^2

Newton-Euler formulation [20]

$$\begin{aligned}\dot{\boldsymbol{\xi}} &= \boldsymbol{Q}\boldsymbol{\omega},\\ \dot{\boldsymbol{\omega}} &= -\boldsymbol{I}^{-1}\boldsymbol{\omega}\times\boldsymbol{I}\boldsymbol{\omega}+\boldsymbol{I}^{-1}\boldsymbol{M}+\boldsymbol{I}^{-1}\boldsymbol{T},\end{aligned} \tag{2}$$

where, $\boldsymbol{\omega} = [p, q, r]^T$ represents the angular velocities in $\mathcal{B}$, and $\boldsymbol{Q}$ is the transformation matrix defined in (3). $\boldsymbol{M}$ and $\boldsymbol{T}$ denote the aerodynamic moment and the external disturbance torque in $\mathcal{B}$ respectively. The inertia tensor $\boldsymbol{I}$ is constant and defined in the body frame.

$$\boldsymbol{Q} = \begin{bmatrix} 1 & s_\phi t_\theta & c_\phi t_\theta \\ 0 & c_\phi & -s_\phi \\ 0 & s_\phi/c_\theta & c_\phi/c_\theta \end{bmatrix}, \tag{3}$$

$$\boldsymbol{I} = \begin{bmatrix} I_{xx} & -I_{xy} & -I_{xz} \\ -I_{xy} & I_{yy} & -I_{yz} \\ -I_{xz} & -I_{yz} & I_{zz} \end{bmatrix}. \tag{4}$$

The abbreviations s_*, c_* and t_* denote, respectively, $sin(*)$, $cos(*)$ and $tan(*)$.

It is assumed that the $X_bO_bZ_b$ plane is the plane of symmetry of the airplane, thus the products of inertia $I_{xy} = I_{yz} = 0$. The detailed aerodynamics of US 25e is described in Appendix A. The general mass and geometry characteristics are given in Table. 1 [21].

III. VIRTUAL ANGULAR ACCELEROMETER

In this section, a virtual angular accelerometer is proposed. The virtual sensor is based on multi-IMUs fusion. The IMUs implementation will be presented. And the extended Kalman filter will be used to fuse the inertial information to estimate the disturbance.

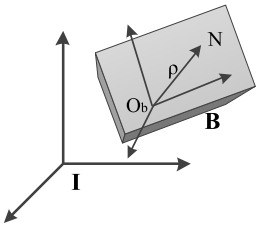

FIGURE 2. Acceleration of a point in rigid body.

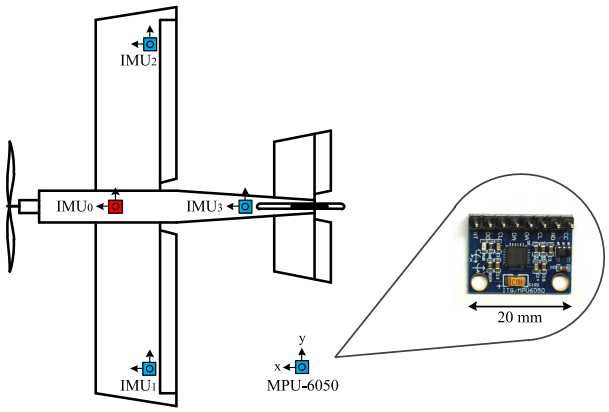

FIGURE 3. The US 25e RC airplane.

A. PROBLEM FORMULATION

A more generalized mechanical formula of (1) can be given as

$$\boldsymbol{a}_N = \boldsymbol{a}_b + \boldsymbol{\alpha}_b \times \boldsymbol{\rho} + \boldsymbol{\omega}_b \times (\boldsymbol{\omega}_b \times \boldsymbol{\rho}) \tag{5}$$

where, N is a point fixed in a free rigid body **B** shown in Fig. 2, $\boldsymbol{a}_N$ denotes the absolute acceleration of N, $\boldsymbol{a}_b$ represents the implicated acceleration (absolute acceleration of the reference point O_b). $\boldsymbol{\rho}$ stands for the relative position O_bN. $\boldsymbol{\alpha}_b$ and $\boldsymbol{\omega}_b$ are the angular acceleration and angular velocity of **B** respectively. It can be seen from (5) that $\boldsymbol{\alpha}_b$ is solvable in the event that $\boldsymbol{a}_N$, $\boldsymbol{a}_b$, $\boldsymbol{\rho}$ and $\boldsymbol{\omega}_b$ are known. Despite the fact that $\boldsymbol{\alpha}_b = \dot{\boldsymbol{\omega}}_b$, it seems that angular acceleration is readily available by differentiating angular velocity measurement. However, phase lag and error are the paradoxical problems faced by researchers.

The MEMS IMU can provide linear acceleration and angular velocity information, which is natural for angular acceleration estimation.

B. IMUS IMPLEMENTATION

In this work, three additional MEMS IMUs marked blue are installed into the airplane illustrated in Fig. 3. Together with the original IMU in the avionics system marked red, there are 4 IMUs embedded in the rigid airframe.

TABLE 2. Installation position of the IMUs.

	IMU_0	IMU_1	IMU_2	IMU_3
Coordinates in $\mathcal{B}$ (m)	(0, 0, 0)	(-0.1, -0.5, 0)	(-0.1, 0.5, 0)	(-0.4, 0, 0)

As a low-cost MEMS IMU designed towards consumer use, the MPU-6050 is often the primary Motion-Tracking device [22]. The MPU-6050 integrated a 3-axis gyroscope and a 3-axis accelerometer in a tiny $4 \times 4 \times 0.9$ mm package, is still popular in open-hardware community. Three MPU-6050 chip modules (IMU1-IMU3) are used in the research, which cost about 10 $. Though the design will increase the expenditure slightly, the benefits are obvious, for example, the redundant measurements enhance the reliability of the avionics system [23]. The locations of the IMUs are given in Table. 2. The orientations of the Sensing Axes are aligned with the Body Axes, which make the installation and calibration easier.

In the work, the MPU-6050 was configured at sample time of 4 ms. Registers DLPF_CFG=1 and SMPLRT_DIV=3. The IMU was tested and the output raw data has statistical properties of $\sigma_{acc} = 0.035$ m/s^2, and $\sigma_{gyro} = 0.12$ °/s.

C. EKF FUSION METHOD

The additional 3 IMUs provide redundant inertial information. To obtain inertial state from the raw measurement data, proper estimation methods must be employed. Least square estimation and Kalman filter are commonly used methods [23]. And to relieve the communication burden and achieve an appropriate estimation accuracy, event-trigger filters may help [7], [13], [24], [31].

From (2) we know that linear acceleration f_b and angular acceleration α_b are all driven by internal and external factors. The external disturbances are usually random and unknown. In state tracking problem, the unknown state is usually modeled as Constant Velocity or Constant Acceleration driven by noise. In this work, CA model is adopted to build the process model. Define the state $\boldsymbol{x}$ as $[\boldsymbol{f}_b, \boldsymbol{\alpha}_b, \boldsymbol{\omega}_b]^T$. The discrete state-functions can be given by

$$\begin{aligned}
\boldsymbol{f}_b(k+1) &= \boldsymbol{f}_b(k) + \boldsymbol{w}_f(k) \\
\boldsymbol{\alpha}_b(k+1) &= \boldsymbol{\alpha}_b(k) + \boldsymbol{w}_\alpha(k) \\
\boldsymbol{\omega}_b(k+1) &= \boldsymbol{\omega}_b(k) + \boldsymbol{\alpha}_b(k) \cdot \Delta t
\end{aligned} \tag{6}$$

where, Δt denotes the sampling time interval, k + 1 and k are indices of the time series. $\boldsymbol{w}_f$ and $\boldsymbol{w}_\alpha$ are process noises driven the states. For a US 25e airplane flying in calm and windy environment, the standard deviation of $\boldsymbol{w}_f$ and $\boldsymbol{w}_\alpha$ may increase up to 10 times according to Dryden Wind Turbulence Model, shown in Table. 3. Since the driven noise changes considerably in different weather conditions, $\sigma(\boldsymbol{w}_f)$ and $\sigma(\boldsymbol{w}_\alpha)$ may be adjusted manually. Moreover, simulation reveals that EKF is robust against the perturbation of the two parameters.

TABLE 3. Process noise characteristic of different turbulent air.

Wind Scale	Wind speed[a] (m/s)	Standard deviation $\sigma(w_f)$ (m/s^2)	Standard deviation $\sigma(w_\alpha)$ (°/s^2)
Light Air	1	0.2	40
Near Gale	15	2	130

[a] Wind speed is measured at 6 m above ground. Note that, the typical flight altitude is set as 100 m above the ground.

From (B-5) in Appendix B, the measurement functions can be obtained as follows,

$$\begin{aligned}
A_{0\,x} &= f_x + \xi_{0\,x} \\
A_{0\,y} &= f_y + \xi_{0\,y} \\
A_{0\,z} &= f_z + \xi_{0\,z} \\
G_{0\,x} &= \omega_x + \zeta_{0\,x} \\
G_{0\,y} &= \omega_y + \zeta_{0\,y} \\
G_{0\,z} &= \omega_z + \zeta_{0\,z} \\
[4pt]A_{1\,x} &= \mathcal{F}_{1x}(f_b, \alpha_b, \omega_b) + \xi_{1\,x} \\
A_{1\,y} &= \mathcal{F}_{1y}(f_b, \alpha_b, \omega_b) + \xi_{1\,y} \\
A_{1\,z} &= \mathcal{F}_{1z}(f_b, \alpha_b, \omega_b) + \xi_{1\,z} \\
G_{1\,x} &= \omega_x + \zeta_{1\,x} \\
G_{1\,y} &= \omega_y + \zeta_{1\,y} \\
G_{1\,z} &= \omega_z + \zeta_{1\,z} \\
[4pt]A_{2\,x} &= \mathcal{F}_{2x}(f_b, \alpha_b, \omega_b) + \xi_{2x} \\
&\vdots \\
G_{3z} &= \omega_z + \zeta_{3z}
\end{aligned} \tag{7}$$

where, $\mathcal{F}_*(f_b, \alpha_b, \omega_b)$ are nonlinear functions. Hence, we obtain 9 linear state-functions (6) and 24(9 nonlinear) measurement functions (7), which can be rewritten as

$$\begin{aligned}
\boldsymbol{x}(k+1) &= \boldsymbol{\Phi}(k+1|k)\boldsymbol{x}(k) + \boldsymbol{w}(k) \\
\boldsymbol{z}(k+1) &= \boldsymbol{h}[x(k+1), k+1] + \boldsymbol{v}(k+1)
\end{aligned} \tag{8}$$

where, $\boldsymbol{x}$ and $\boldsymbol{z}$ are the states and measurements respectively, $\boldsymbol{\Phi}$ represents the state transfer matrix, $\boldsymbol{h}[*]$ denotes the nonlinear measurement functions. $\boldsymbol{w}$ and $\boldsymbol{v}$ stand for the process and measurement noise vectors, which are assumed as zero mean white noises satisfying

$$\begin{aligned}
E[\boldsymbol{w}(k)] &= E[\boldsymbol{v}(k)] = \boldsymbol{0} \\
E\left[\boldsymbol{w}(k)\boldsymbol{w}^T(j)\right] &= \boldsymbol{Q}(k)\delta_{kj} \\
E\left[\boldsymbol{v}(k)\boldsymbol{v}^T(j)\right] &= \boldsymbol{R}(k)\delta_{kj} \\
E\left[\boldsymbol{w}(k)\boldsymbol{v}^T(j)\right] &= \boldsymbol{0}, \quad \delta_{kj} = \begin{cases} 1, & k = j \\ 0, & k \neq j \end{cases}
\end{aligned} \tag{9}$$

The fusion of the 24 IMU outputs is performed by Extended Kalman filter (EKF) which is suitable for the nonlinear filtering. The EKF approximates a nonlinear function by the Taylor series expansion, retaining first-order term and

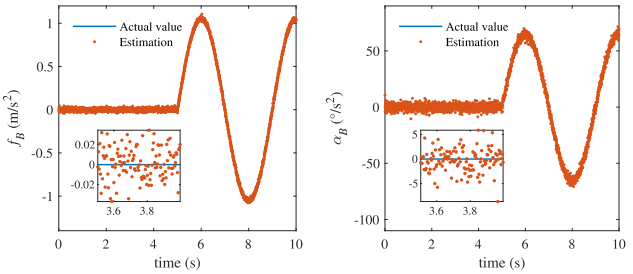

FIGURE 4. The EKF fusion results: (a) Specific force;(b) Angular acceleration.

omitting second-order and high-order terms. The Jacobian matrix is defined by

$$\boldsymbol{H} = \frac{\partial \boldsymbol{h}}{\partial \boldsymbol{x}}$$

The discrete extended Kalman filter equations are presented as follows,

$$\hat{\boldsymbol{x}}(k+1|k) = \boldsymbol{\Phi}(k+1|k)\hat{\boldsymbol{x}}(k|k) \tag{10}$$

$$\boldsymbol{P}(k+1|k) = \boldsymbol{\Phi}(k+1|k)\boldsymbol{P}(k|k)\boldsymbol{\Phi}^{\mathrm{T}}(k+1|k)+\boldsymbol{Q}(k+1) \tag{11}$$

$$\boldsymbol{H}(k+1) = \left.\frac{\partial h}{\partial x}\right|_{x=\hat{x}(k+1|k)} \tag{12}$$

$$\boldsymbol{K}(k+1) = \boldsymbol{P}(k+1|k)\boldsymbol{H}^{\mathrm{T}}(k+1) \left[\boldsymbol{H}(k+1)\boldsymbol{P}(k+1|k)\boldsymbol{H}^{\mathrm{T}}(k+1)+\boldsymbol{R}(k+1)\right]^{-1} \tag{13}$$

$$\hat{\boldsymbol{x}}(k+1|k+1) = \hat{\boldsymbol{x}}(k+1|k) + \boldsymbol{K}(k+1)[\boldsymbol{Z}(k+1)-\boldsymbol{h}[\hat{\boldsymbol{x}}(k+1|k), k+1]] \tag{14}$$

$$\boldsymbol{P}(k+1|k+1) = [\boldsymbol{I}-\boldsymbol{K}(k+1)\boldsymbol{H}(k+1)]\boldsymbol{P}(k+1|k) \tag{15}$$

A schematic of the EKF algorithm is summarized in Algorithm. 1.

Algorithm 1 EKF Algorithm

Require: $\hat{\boldsymbol{x}}(0|0)$, $\boldsymbol{P}(0|0)$

1: **for** $k = 0$ to k_{end} **do**
2: Estimate $\hat{\boldsymbol{x}}(k+1|k)$ by (10)
3: Estimate $\boldsymbol{P}(k+1|k)$ by (11)
4: Calculate $\boldsymbol{H}(k+1)$ by (12)
5: Calculate $\boldsymbol{K}(k+1)$ by (13)
6: Update $\hat{\boldsymbol{x}}(k+1|k+1)$ by (14)
7: Update $\boldsymbol{P}(k+1|k+1)$ by (15)
8: **end for**

Fig. 4 shows the results of the multi-IMUs fusion. The angular acceleration can be measured by the virtual sensor. The accuracy of the virtual sensor $\sigma(\alpha_b) = 2.4\ °/s^2$. The accuracy of the IMU measurements is improved, shown in Table. 4.

TABLE 4. Comparison of raw data and fusion results.

MPU-6050	σ_f (m/s^2)	σ_α (°/s^2)	σ_ω (°/s)
Raw data	0.035	×	0.12
Fusion result	0.015	2.4	0.025

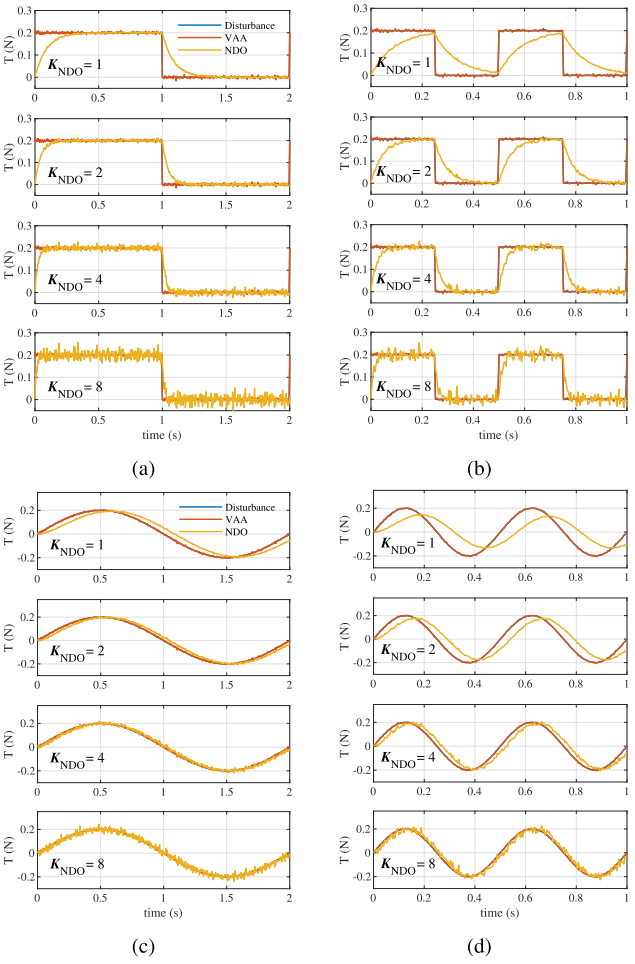

FIGURE 5. The estimation results of VAA (Virtual angular accelerometer) and NDO (nonlinear disturbance observer) against two forms of disturbances: (a) Square wave disturbance torque of frequency 0.5 Hz; (b) Square wave disturbance torque of frequency 2 Hz; (c) Sine wave disturbance torque of frequency 0.5 Hz; (d) Sine wave disturbance torque of frequency 2 Hz. (The observer gain K of NDO is increased from top to bottom. The EKF has the same initial values $\hat{x}(0|0)$ and $P(0|0)$. Because of the inherent dynamic process, the model-based NDO degrades when estimating the fast time-varying disturbances. The sensor-based VAA has barely no time-delay and phase lag that the rad VAA line and the blue disturbance line are almost coincident.)

D. COMPARISON WITH NDO

To show the good performance of the Virtual Angular Accelerometer (VAA), a model-based nonlinear disturbance observer (NDO) is introduced to compare with the VAA. The detailed algorithm of NDO is listed in Appendix C. It can be seen clearly from Fig. 5(a) and (b) that model-based NDO has serious time delay for square wave form disturbance. And Fig. 5(c) and (d) show the estimation phase lag for sine wave form disturbance. The disturbances have frequencies

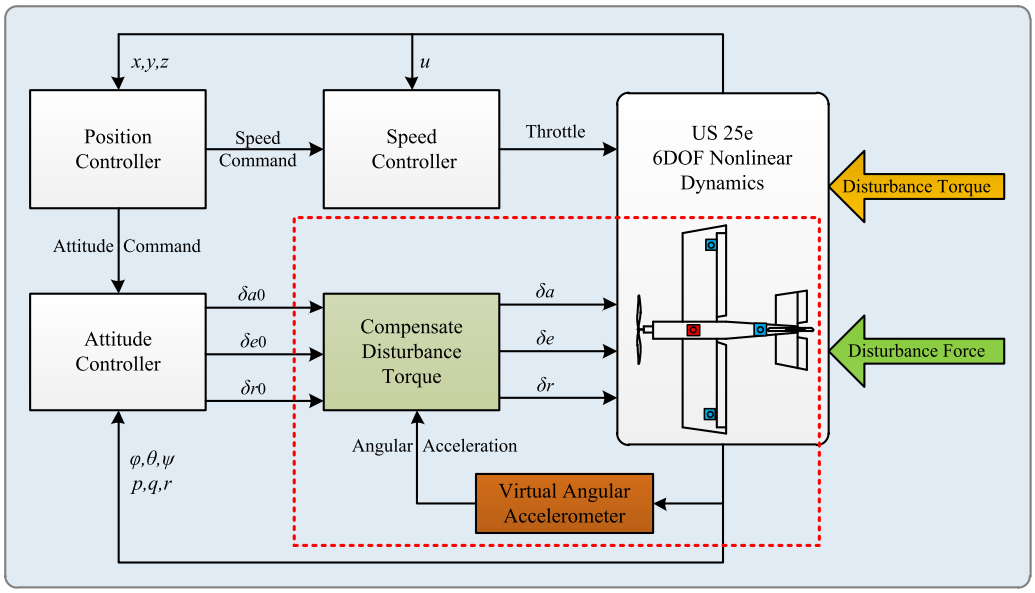

FIGURE 6. US 25e flight control scheme.

of 0.5 Hz and 2 Hz. The higher the frequency of the disturbance is, the greater the NDO phase lag is. The observer gain $\boldsymbol{K}_{NDO}$ is increased from 1 to 8 labeled in each sub-figure from top to bottom. The time delay and phase lag are decreased when increasing $\boldsymbol{K}_{NDO}$. Although the time delay and phase lag of NDO may be improved by increasing the observer gain, the observation noise is increased dramatically. The rapidity and accuracy of NDO are a pair of contradictions. The NDO seems not suitable for estimation of fast time-varying disturbances because of the precondition $\dot{\boldsymbol{d}} \approx 0$. However, the VAA (marked red in the figures) maintains very short time delay and phase lag, and the observation noise is relatively small.

In further study, the NDO shows good performance in estimating slowly time-varying and constant disturbances. The reason why VAA has high response frequency is that the MEMS IMU has a output frequency up to 1000Hz, which means the VAA has a time delay of milliseconds. The defect of VAA is that it needs additional hardware devices and structural designs, and the 24-dimensional EKF consumes more computing and power resources. However, the NDO has a relatively simple structure.

IV. ENHANCED ATTITUDE CONTROL SCHEME

A. CONTROL STRUCTURE

Fixed-wing small UAV, such as US 25e, has three aerodynamic control surfaces - aileron δ_a, elevator δ_e, and rudder δ_r, to generate roll, pitch and yaw torques respectively, and a propeller to generate thrust force. Obviously, the attitude subsystem is fully actuated [25]. The full-actuated property of the attitude subsystem guarantees that the external disturbance torque might be compensated precisely and immediately. Our objective is to design a flight controller to enhance the attitude subsystem stability.

A general control scheme of US 25e is illustrated in Fig. 5. The enhancement structure, high-lighted by a red-dotted box, is cascaded to the conventional flight controller. The structure can be employed to linear or nonlinear flight control methods to enhance attitude stability. δ_{a0}, δ_{e0}, and δ_{r0} are initial controller command. Here, we assume that the disturbance $\boldsymbol{T}$ is bounded. If the disturbance is beyond the control authority of the small UAV, it is difficult to maintain a stable flight and not the problem to be solved in this paper.

In order to reduce the airplane angular vibration, the key is to estimate the disturbance torque and compensate precisely. From (2), we can get $\boldsymbol{T} = \boldsymbol{I}\dot{\boldsymbol{\omega}} - \boldsymbol{\omega} \times \boldsymbol{I}\boldsymbol{\omega} - \boldsymbol{M}$. Angular acceleration $\boldsymbol{\alpha_b}$ can be estimated accurately with little phase lag, which lays the foundation of estimating disturbance torque effectively. The estimation of disturbance torque $\hat{\boldsymbol{T}}$ can be given as

$$\hat{\boldsymbol{T}} = \boldsymbol{I}\hat{\boldsymbol{\alpha}}_b - \boldsymbol{\omega} \times \boldsymbol{I}\boldsymbol{\omega} - \boldsymbol{M}. \tag{16}$$

A noticeable way to compensate the disturbance torque is to deflect the control surface to counteract the torque as depicted in Fig. 6, where B is the control allocation matrix defined in (17). A first order servo model is incorporated in the compensation algorithm to eliminate the algebraic loop, where a pre-filter is utilized to solve the problem [26].

$$\begin{aligned} \boldsymbol{B} &= \frac{\partial \boldsymbol{M}}{\partial\,(\delta_a, \delta_e, \delta_r)} \\ &= \bar{q}S \begin{bmatrix} b \\ \bar{c} \\ b \end{bmatrix} .* \begin{bmatrix} C_l^{\delta_a} & 0 & C_l^{\delta_a} \\ 0 & C_m^{\delta_e} & 0 \\ C_n^{\delta_r} & 0 & C_n^{\delta_r} \end{bmatrix}. \end{aligned} \tag{17}$$

For attitude subsystem (2), the control input $\boldsymbol{u}$ can be designed as

$$\boldsymbol{u} = \boldsymbol{u}_f + \boldsymbol{u}_c \tag{18}$$

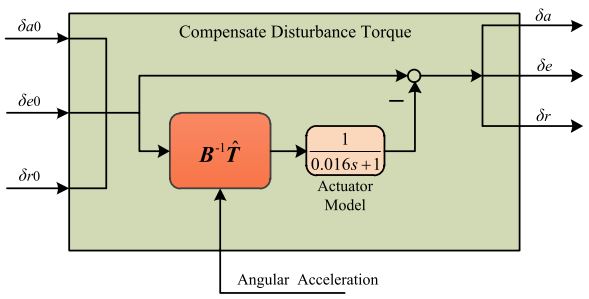

FIGURE 7. Disturbance compensation.

where, $\boldsymbol{u}_f$ and $\boldsymbol{u}_c$ are the feedback and compensation actions, respectively. The term $\boldsymbol{u}_c$ can be chosen as $-\hat{\boldsymbol{T}}$ to compensate the disturbance.

Here we employ backstepping method to design a feedback control signal $\boldsymbol{u}_f$ as an example [29], [36]. Define $\boldsymbol{x}_1 = \boldsymbol{\xi}$ and $\boldsymbol{x}_2 = \boldsymbol{\omega}$. The longitudinal kinetic equations (2) can be rewritten as a more general strict feedback form:

$$\begin{aligned} \dot{\boldsymbol{x}}_1 &= \boldsymbol{g}_1 \boldsymbol{x}_2 \\ \dot{\boldsymbol{x}}_2 &= \boldsymbol{f}_2 + \boldsymbol{g}_2 \boldsymbol{u} + \boldsymbol{g}_2 \boldsymbol{T} \end{aligned} \tag{19}$$

where, $\boldsymbol{g}_1 = \boldsymbol{Q}, \boldsymbol{f}_2 = -\boldsymbol{I}^{-1}\boldsymbol{\omega} \times \boldsymbol{I}\boldsymbol{\omega}$ and $\boldsymbol{g}_2 = \boldsymbol{I}^{-1}$. We design the enhanced control law as:

$$\boldsymbol{u} = \boldsymbol{g}_2^{-1}(-\boldsymbol{f}_2 + \dot{\boldsymbol{x}}_{2d} - \boldsymbol{g}_1^T \boldsymbol{z}_1 - \boldsymbol{c}_2 \boldsymbol{z}_2) - \hat{\boldsymbol{T}} \tag{20}$$

where, $\boldsymbol{x}_{2d} = \boldsymbol{g}_1^{-1}(\dot{\boldsymbol{x}}_{1d} - \boldsymbol{c}_1 \boldsymbol{z}_1)$. $\boldsymbol{z}_1 = \boldsymbol{x}_1 - \boldsymbol{x}_{1d}$ and $\boldsymbol{z}_2 = \boldsymbol{x}_2 - \boldsymbol{x}_{2d}$ are tracking errors. $\boldsymbol{c}_1$ and $\boldsymbol{c}_2$ are designed control gains.

It can be seen from the preceding analysis that the disturbance torque can be compensated by deflecting the flaps directly. However, it might not be easy for the case of disturbance force. The components of aerodynamic force generated by the flaps are much smaller than that by changing flow angles, for instance, $C_L^{\delta_e} < 0.01 C_L^{\alpha}$, which is why the outer loop subsystem is under actuated. To compensate disturbance force for a conventional airplane, its attitude must be changed firstly. In other words, it is almost impossible to compensate external force without changing the attitude.

B. STABILITY ANALYSIS

The EKF is a widely-used mature tool in information fusion. The robustness and effectiveness of the filter are verified in many applications. Considering the nonlinear stochastic system given by (8) and the EKF as stated in (10) to (15), the estimation error of EKF is stochastic stability, if we elaborately choose the initial values $\hat{\boldsymbol{x}}(0|0)$ and $\boldsymbol{P}(0|0)$ [37].

For the convenience of control stability analysis, the compensation term $\boldsymbol{u}_c$ is modified as follows:

$$\boldsymbol{u}_c = -sat(\hat{\boldsymbol{T}}), \quad sat(\hat{\boldsymbol{T}}) = \begin{cases} T_{max}\boldsymbol{I}_{3\times 3}, & \|\hat{\boldsymbol{T}}\| > T_{max} \\ \hat{\boldsymbol{T}} & \\ -T_{max}\boldsymbol{I}_{3\times 3}, & \|\hat{\boldsymbol{T}}\| < T_{max} \end{cases} \tag{21}$$

where, T_{max} is a constant that assumed as the upper bound of the disturbance. The modification do not change the estimator performance. Thus, the synthesis control law (20) is rewritten as

$$\boldsymbol{u} = \boldsymbol{g}_2^{-1}(-\boldsymbol{f}_2 + \dot{\boldsymbol{x}}_{2d} - \boldsymbol{g}_1^T \boldsymbol{z}_1 - \boldsymbol{c}_2 \boldsymbol{z}_2) - sat(\hat{\boldsymbol{T}}) \tag{22}$$

Theorem 1: Consider the controller (22), the estimator (21) and the attitude system described by (19) suffering bounded disturbance. The closed-loop signals in (23) are bounded and $\boldsymbol{z}_i$ converges to a bounded neighborhood of $\boldsymbol{z}_i = 0$.

Proof: Select the following Lyapunov function:

$$V_s = \frac{1}{2}\boldsymbol{z}_1^T \boldsymbol{z}_1 + \frac{1}{2}\boldsymbol{z}_2^T \boldsymbol{z}_2 \tag{23}$$

The derivative of V is calculated as

$$\begin{aligned} \dot{V}_s &= \boldsymbol{z}_1^T \dot{\boldsymbol{z}}_1 + \boldsymbol{z}_2^T \dot{\boldsymbol{z}}_2 \\ &= \boldsymbol{z}_1^T (\boldsymbol{g}_1 \boldsymbol{x}_2 - \dot{\boldsymbol{x}}_{1d}) + \boldsymbol{z}_2^T (\boldsymbol{f}_2 + \boldsymbol{g}_2 \boldsymbol{u} + \boldsymbol{g}_2 \boldsymbol{T} - \dot{\boldsymbol{x}}_{2d}) \end{aligned} \tag{24}$$

Combing (22), the derivative of V_s can be further calculated as

$$\dot{V}_s = -\boldsymbol{z}_1^T \boldsymbol{c}_1 \boldsymbol{z}_1 - \boldsymbol{z}_2^T \boldsymbol{c}_2 \boldsymbol{z}_2 + \boldsymbol{z}_2^T \boldsymbol{g}_2 \tilde{\boldsymbol{T}} \tag{25}$$

where, the disturbance estimation error $\tilde{\boldsymbol{T}} = \boldsymbol{T} - sat(\hat{\boldsymbol{T}})$. It is obvious that $\tilde{\boldsymbol{T}}$ is bounded and $\|\tilde{\boldsymbol{T}}\| < 2T_{max}$. Equation (25) can be rewritten as the following form:

$$\dot{V}_s \leqslant -cV_s + \rho \tag{26}$$

where, $c = min\{\boldsymbol{c}_1, \boldsymbol{c}_2\}$, $\rho = \boldsymbol{z}_2^T \boldsymbol{g}_2 \tilde{\boldsymbol{T}}$. Therefore, V_s converges exponentially until $V_s \leqslant \frac{\rho}{c}$ [36].

V. SIMULATION RESULTS AND ANALYSIS

In this section, the effectiveness and the robustness of the proposed hierarchical enhanced control structure were evaluated through 3 simulation cases. The general descriptions of the SUAV are given in Table. 1 and Appendix A. The initial conditions were the same for the different simulation cases with the initial position $\boldsymbol{\chi}(0) = [0, 0, -100\ \text{m}]^T$ and initial Euler angles $\boldsymbol{\xi}(0) = [0, 2^\circ, 0]^T$. The flight speed controller was utilized to maintain the initial forward speed $u(0) = 16$ m/s. The initial angular velocities were set to zero.

To show the excellent performance of the enhanced attitude control scheme, its performance was compared to the basic controller. We designed two basic controllers: a linear PID controller and a nonlinear backstepping controller (BS). The PID controller had a three-channel structure. The BS controller was presented at IV-A. The basic controllers (PID, BS) and the enhanced attitude controllers (PID+VAA, BS+VAA) shared the same control parameters. To compare the disturbance rejection performance, a NDO based Robust controller (RC, RC+NDO, and RC+VAA) was also studied (Refer to Appendix C).

The three controllers parameters were summarized in Table. 5. The rise times of the three channels were 0.15 s, 0.08 s, and 0.17 s for pitch, roll, and yaw PID controllers, respectively. The basic BS control gains ($\boldsymbol{c}_1$ and $\boldsymbol{c}_2$) and the basic RC gains ($\boldsymbol{\lambda}_1$ and $\boldsymbol{\lambda}_2$) were tuned to ensure that the

TABLE 5. The parameters of PID, BS, and RC controllers.

PID controller, [Kp, Ki, Kd]			Backstepping controller (BS)		Robust controller (RC)		
Roll Channel	Pitch Channel	Yaw Channel	Control gain $\boldsymbol{c}_1$	Control gain $\boldsymbol{c}_2$	NDO gain $\boldsymbol{K}$	Control gain $\boldsymbol{\lambda}_1$	Control gain $\boldsymbol{\lambda}_2$
[4.4, 7, 0.37]	[-5, -9, -0.09]	[-5.2, -9, -0.5]	[14.5, 23, 5.5]	[14.5, 23, 5.5]	[2, 4, 6]	[4, 8, 2]	[3, 8, 2]

TABLE 6. Improvement of the attitude tracking performance.

TE	PID control			Backstepping control			Robust control				
	basic PID	PID+VAA	Improvement	basic BS	BS+VAA	Improvement	basic RC	RC+VAA	Improvement	RC+NDO	Improvement
Roll Channel	0.83	0.16	**80.7%**	0.62	0.08	**87.1%**	0.62	0.06	**90.3%**	0.14	**77.4%**
Pitch Channel	0.35	0.30	**14.3%**	0.65	0.12	**81.5%**	0.65	0.09	**86.2%**	0.18	**72.3%**
Yaw Channel	0.54	0.33	**38.9%**	0.63	0.04	**93.7%**	0.64	0.05	**92.2%**	0.09	**85.9%**

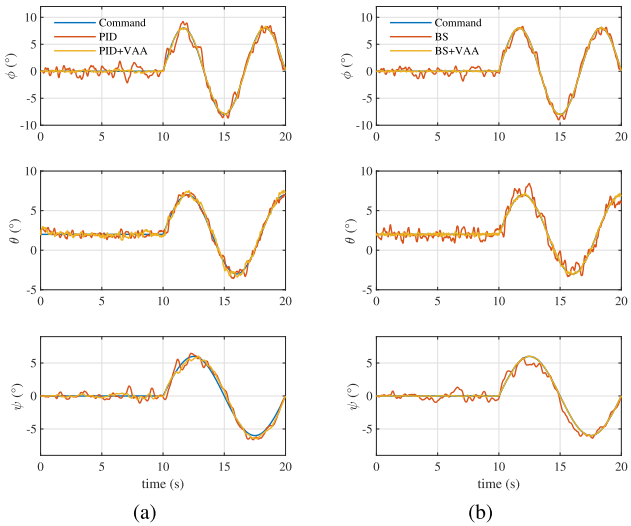

FIGURE 8. Euler angle tracking performance: (a) PID controller; (b) Backstepping controller (BS).

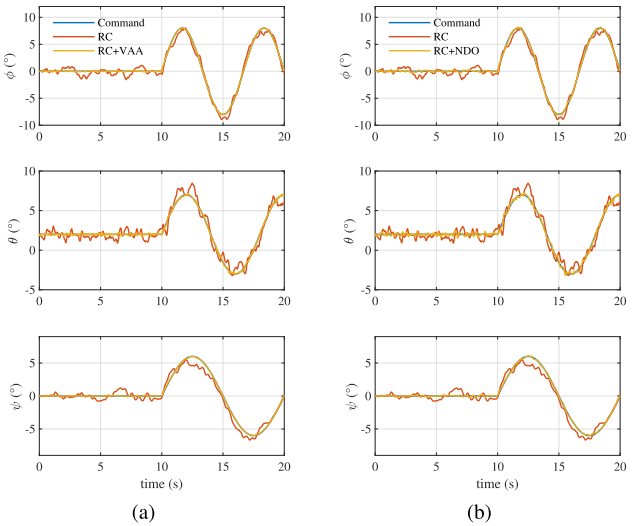

FIGURE 9. Angle command tracking performance: (a) VAA based robust control; (b) NDO based robust control.

3 controllers had similar tracking performance ($TE \approx 0.65$), seeing also Table. 6.

The MPU-6050 outputs were simulated by adding Gaussian random numbers to actual values. The standard deviations of the random numbers were based on experiments in III: $\sigma_{acc} = 0.035$ m/s^2, and $\sigma_{gyro} = 0.12°$/s.

In order to quantify the attitude tracking performance, a state tracking root-mean-square error *TE* is defined as

$$TE(x) = \sqrt{\frac{1}{T}\int_0^T [x(t) - x_c(t)]^2\, dt}$$

where, $x(t)$ and $x_c(t)$ are the state and command respectively. Obviously, the smaller the *TE* is, the better the tracking performance is. The following simulation cases were carried out using Matlab/Simulink at a fixed time step of 4 ms. The wind speed at 6 m (20 feet) above ground was selected as 15.4 m/s (30 knots), which represented moderate turbulent environment according to Dryden Wind Turbulence Model.

A. TRACKING EULERIAN ANGLE COMMAND

Fig. 8 showed the Eulerian angle tracking performance of the PID and backstepping controllers. Two kinds of Eulerian command were drawn in the same figure, marked blue: constant value command in 0-10 s and sinusoidal waveform command in 10-20 s. The attitude responses of the basic controllers (PID, BS) were the red lines. And the enhanced attitude responses (PID+VAA, BS+VAA) were drawn in yellow. Even though both the basic controllers can keep track with the command, the tracking performance of the enhanced attitude controllers were much better.

As shown in Table. 6, the enhanced attitude controllers PID+VAA and BS+VAA achieved great improvements against the basic controllers. For PID controller, the biggest improvement in tracking performance had been observed in roll channel to about 81%, yet the improvement in pitch channel seemed less. That might be because the conventional pitch channel PID controller already had a relatively good performance. The enhanced backstepping controller showed accordant improvement to about 90% in roll, pitch, and yaw channels.

To compare VAA with NDO, the Robust controller (RC) was simulated in 3 modes: the basic RC, the RC+VAA, and RC+NDO. The results were depicted in Fig. 9. Both the RC+VAA and RC+NDO, compared to the basic RC, can increase attitude tracking accuracy. The detailed improvements were presented in Table. 6. It can be seen that the VAA based RC is better than the NDO based RC.

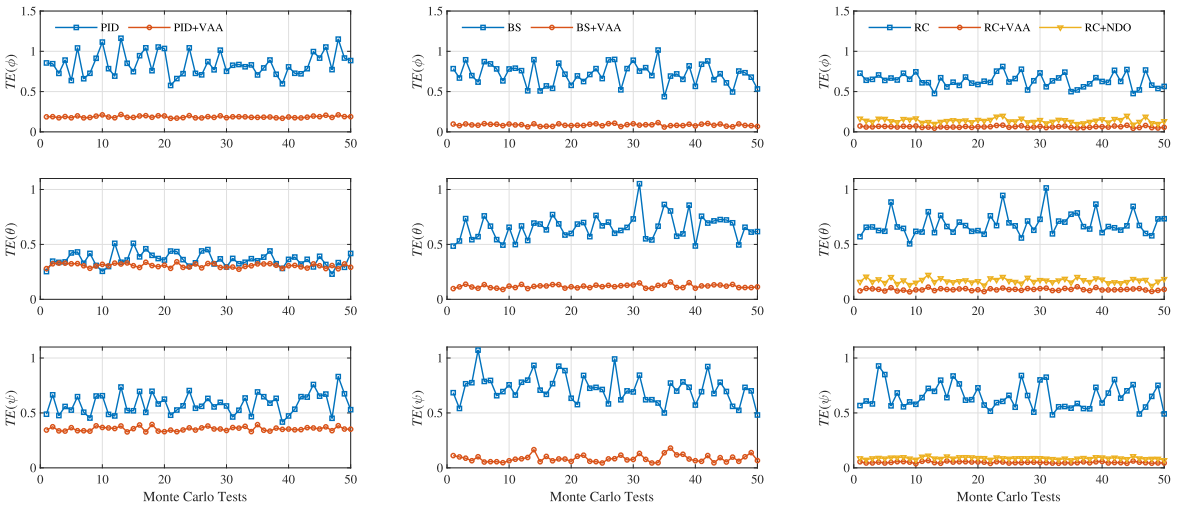

FIGURE 10. Fifty times Monte Carlo tests: (a) PID control; (b) Backstepping control; (c) Robust control. (The lower the line is, the better the performance is.)

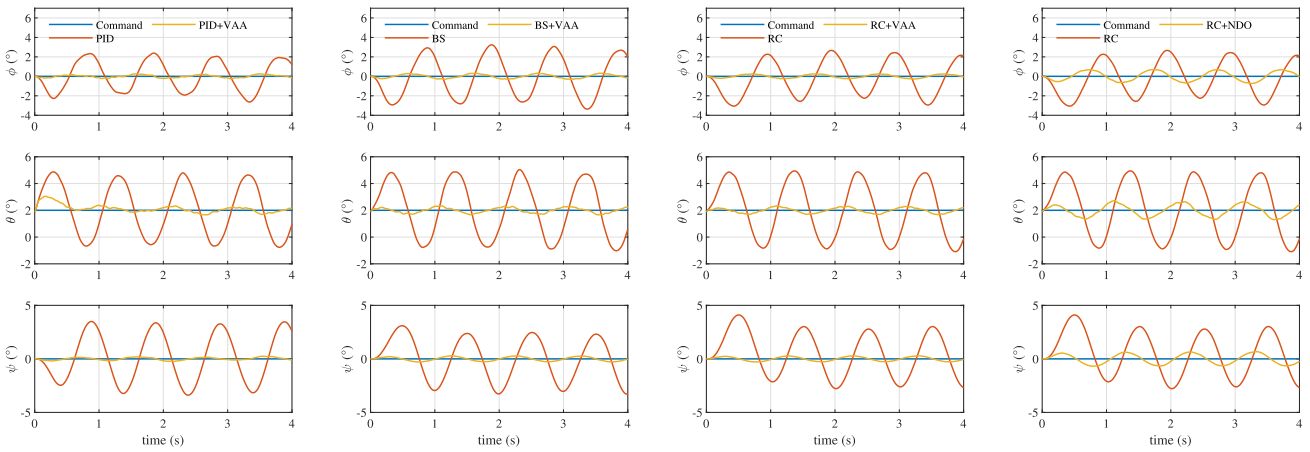

FIGURE 11. Attitude responses against sine wave torque: (a) PID control; (b) Backstepping control; (c) Robust control and VAA based Robust control; (d) Robust control and NDO based Robust control.

B. ROBUSTNESS TESTS

To verify the robustness of the enhanced control strategy, the model uncertainties were introduced in the simulation. The inertia I and aerodynamic C perturbations and IMU installation ρ errors were listed below:

$$\begin{cases} \Delta I_* = \pm 20\% I_* \\ \Delta C_* = \pm 20\% C_* \\ \Delta \rho_* = \pm 2\text{cm} \end{cases}$$

The results of 50 times Monte Carlo experiments were depicted in Fig. 10. It clearly revealed that the enhanced controllers decreased the root-mean-square error TE and improved the control performance in almost all Monte Carlo tests. Furthermore, the enhanced controllers showed stronger robustness against the uncertainties. The blue lines showed the robustness of basic controllers and the red lines for enhanced controllers. The red lines were lower and less fluctuant than the blues lines. Fig. (c) showed the comparison of VAA and NDO. The both could improve the performance and robustness of the basic RC controller. The VAA based RC was a little better than the NDO based RC.

C. FLIGHT WITH DISTURBANCE TORQUE

In this case, sinusoidal and square waveform disturbance torques were involved in the flight to exam the enhanced controller performance. The sine wave torque $\boldsymbol{T}_{sine}$ was given by

$$\boldsymbol{T}_{sine} = \begin{bmatrix} -1.2\sin(2\pi t) \\ 4\sin(2\pi t) \\ 0.7\sin(2\pi t) \end{bmatrix} \text{Nm}$$

where, the amplitudes (1.2, 4, 0.7) were of the same order of magnitude as the control authority. The square wave disturbances were set as amplitudes of (1.2, 4, 0.7), period of 1s, and duty cycle of 50%.

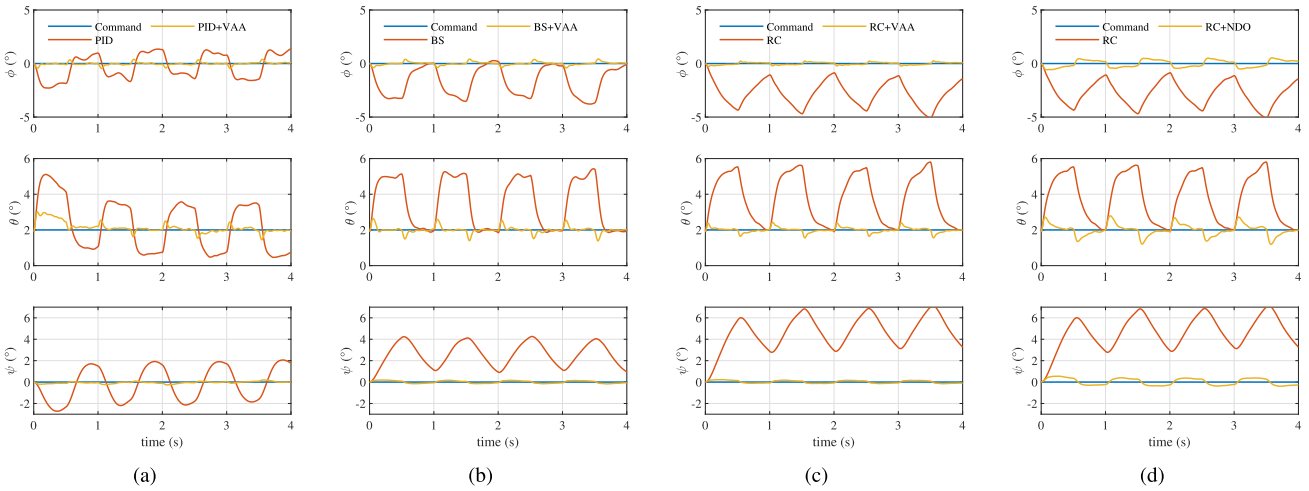

FIGURE 12. Attitude responses against square wave torque: (a) PID control; (b) Backstepping control; (c) Robust control and VAA based Robust control; (d) Robust control and NDO based Robust control.

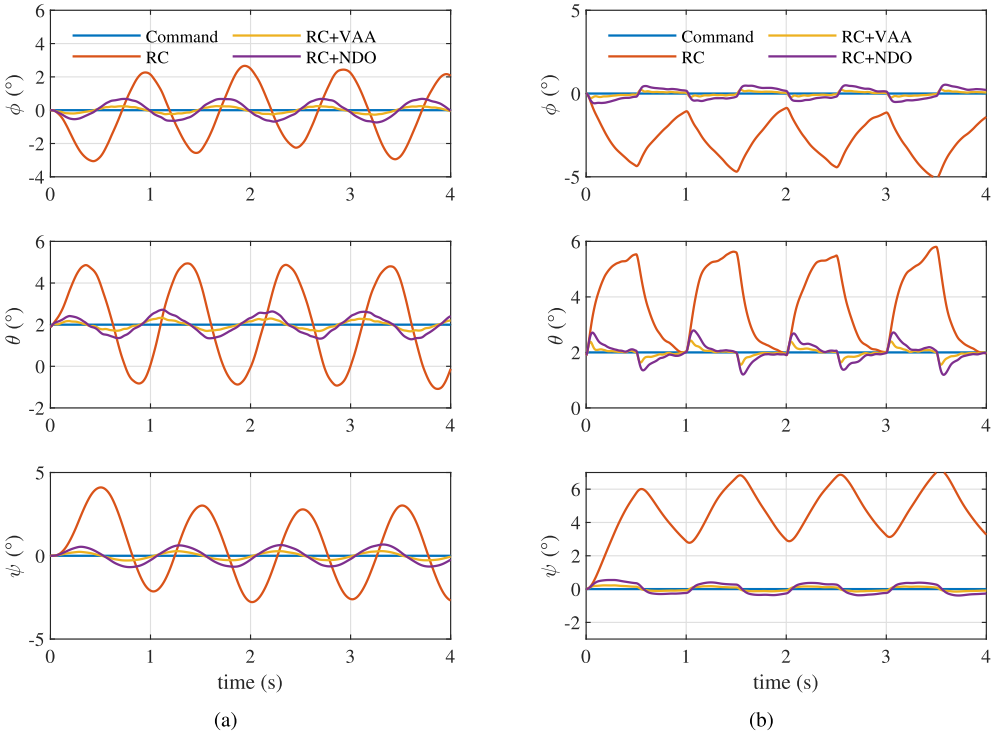

FIGURE 13. Performance of Robust controller against disturbance torque: (a) Attitude responses of basic Robust controller, VAA based Robust controller, and NDO based Robust controller against sine wave disturbance; (b) Attitude responses of basic Robust controller, VAA based Robust controller, and NDO based Robust controller against square wave disturbance.

As shown in Fig. 11 and 12, it was easy to see that the disturbance rejection performance of VAA based controllers were much better than the basic ones. The attitudes under enhanced attitude controllers were almost unaffected by disturbance torque, while it seemed more susceptible for those under the basic controllers.

Fig. 13(a) and 13(b) gave a close look at the performance of the Robust controller against sine wave and square wave disturbances respectively. Both the VAA based Robust control and the NDO based Robust control, compared with the basic Robust control, showed good disturbance rejection performance. Nevertheless, the enhanced scheme controller (RC+VAA) was better than the NDO based Robust controller (RC+NDO).

To show the performance of enhanced attitude control scheme, the comparison of BS+VAA and RC+NDO was

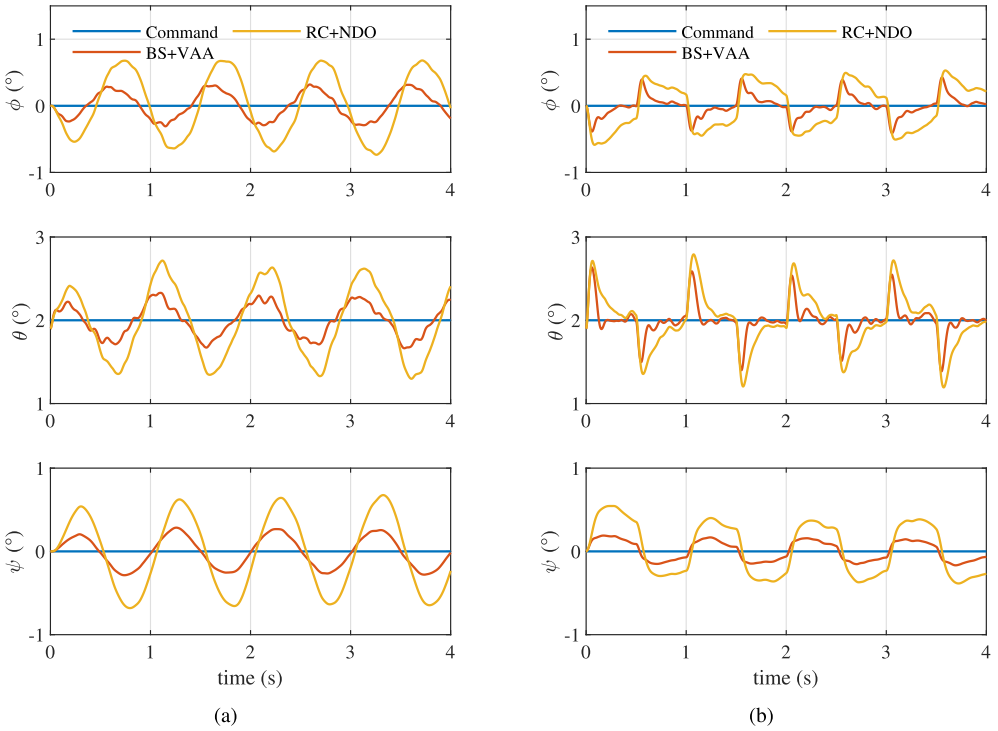

FIGURE 14. Comparison of Enhanced attitude control (BS+VAA) and NDO based control (RC+NDO) against disturbance torque: (a) Attitude responses against sine wave disturbance; (b) Attitude responses against square wave disturbance.

illustrated in Fig. 14. The enhanced attitude controller showed a better performance than the commonly studied NDO based controller in the presence of fast time-varying disturbances. When subjected to quasi-constant disturbance, they had similar performance.

VI. CONCLUSIONS AND FUTURE WORK

In this paper, an enhanced attitude control scheme based on multi-IMUs fusion is proposed for small unmanned aerial vehicles. Three simulation cases are conducted to validate the enhanced flight control performance against turbulence, uncertainties and disturbances. As a distinctive feature, three additional MEMS IMUs, installed off the mass center, are fused to estimate angular acceleration and external disturbance by employing the extended Kalman filter. The developed fusion method shows efficient and reliable performance for disturbance estimation. It can be seen from these simulation results that the enhanced controllers are effective in accomplishing output tracking goals while being robust against uncertainties and disturbances during flight. The enhanced scheme is compatible with linear and nonlinear control methods.

This work is based on a rigid body assumption. The elastic vibration of the airframe may influence the accelerometer output. In future work, we may take into account the flexibility of the airframe.

APPENDIX A
US 25E AERODYNAMICS

The aerodynamic forces $[F_x, F_y, F_z]$ and moments $[M_x, M_y, M_z]$ in body frame $\mathcal{B}$ are defined by

$$\begin{aligned} F_x &= \bar{q}SC_x \\ F_y &= \bar{q}SC_y \\ F_z &= \bar{q}SC_z \end{aligned} \tag{A-1}$$

$$\begin{aligned} M_x &= \bar{q}SbC_l \\ M_y &= \bar{q}S\bar{c}C_m \\ M_z &= \bar{q}SbC_n \end{aligned} \tag{A-2}$$

where, $\bar{q}$ is the dynamic pressure. C_x, C_y, C_z and C_l, C_m, C_n are the aerodynamic coefficients given by

$$\begin{aligned} C_x &= C_L\sin(\alpha) - C_D\cos(\alpha) \\ C_y &= C_y^{\beta}\beta + C_y^{\delta_r}\delta_r + \left(C_y^{p}p + C_y^{r}r\right)b/2V \\ C_z &= -C_L\cos(\alpha) - C_D\sin(\alpha) \end{aligned} \tag{A-3}$$

$$\begin{aligned} C_l &= C_l^{\beta}\beta + C_l^{\delta_j}\delta_a + C_l^{\delta_r}\delta_r + \left(C_l^{p}p + C_l^{r}r\right)b/2V \\ C_m &= C_m^{0} + C_m^{\alpha}\alpha + C_m^{\delta_e}\delta_e + \left(C_m^{\dot{\alpha}}\dot{\alpha} + C_m^{q}q\right)\bar{c}/2V \\ C_n &= C_n^{\beta}\beta + C_n^{\delta_a}\delta_a + C_n^{\delta_r}\delta_r + \left(C_n^{p}p + C_n^{r}\right)b/2V \\ C_L &= C_L^{0} + C_L^{\alpha}\alpha + C_L^{\delta_e}\delta_e + \left(C_L^{\dot{\alpha}}\dot{\alpha} + C_L^{q}q\right)\bar{c}/2V \end{aligned} \tag{A-4}$$

$$C_D = C_D^{0} + C_D^{\delta_e}\delta_e + C_D^{\delta_r}\delta_r + \left(C_L + C_{Lmin}\right)/\pi eAR \tag{A-5}$$

TABLE 7. US 25e nominal aerodynamic values.

C_L^0	0.23	C_L^α	4.58
$C_L^{\delta_e}$	0.13	$C_L^{\dot{\alpha}}$	1.97
C_L^q	7.95	C_D^0	0.043
$C_D^{\delta_e}$	0.014	$C_D^{\delta_r}$	0.03
$C_D^{\delta_a}$	0.03	C_Y^β	-0.83
$C_Y^{\delta_r}$	0.191	C_m^0	0.135
C_m^α	-1.5	$C_m^{\delta_e}$	-1.13
$C_m^{\dot{\alpha}}$	-10.4	C_m^q	-50.8
C_n^{beta}	0.034	$C_n^{\delta_a}$	-0.012
$C_n^{\delta_r}$	-0.035	C_n^p	-0.075
C_n^r	-0.41	C_l^{beta}	-0.04
$C_l^{\delta_a}$	0.068	$C_l^{\delta_r}$	0.017
C_l^p	-0.41	C_l^r	0.4
I_{xx}	0.089	I_{yy}	0.144
I_{zz}	0.162	I_{xz}	0.014

In (A-1)-(A-5), δ_a, δ_e, and δ_r are the aileron, elevator, and rudder deflection angles respectively. V is the airspeed.

The aerodynamic data of US 25e is presented in Table. 7. The nominal coefficients are from Paw's work [27]. These parameters were refined by flight test parameter identification.

APPENDIX B
IMU MEASUREMENT MODEL

The MPU-6050 IMU output three orthogonal angular velocity measurements and three orthogonal linear acceleration measurements. There is little correlation between angular measurement and IMU location in a free-moving rigid object, while linear acceleration measurement is strongly affected by the sensor position.

Note that, accelerometers are basically measuring the specific force $\boldsymbol{f}$. The relationship between $\boldsymbol{f}$ and the absolute acceleration $\boldsymbol{a}$ at point N can be given by $\boldsymbol{f}_N = \boldsymbol{a}_N - \boldsymbol{g}$, where $\boldsymbol{g}$ is the gravitational acceleration [28], and accordingly, the specific force at center of mass $\boldsymbol{f}_b$ equals $\boldsymbol{a}_b - \boldsymbol{g}$. Combing (5), $\boldsymbol{f}_N$ can be rewritten as

$$\boldsymbol{f}_N = \boldsymbol{f}_b + \boldsymbol{\alpha}_b \times \boldsymbol{\rho} + \boldsymbol{\omega}_b \times (\boldsymbol{\omega}_b \times \boldsymbol{\rho}) \tag{B-1}$$

Supposing that an accelerometer is located at position N (represented by vector $\boldsymbol{\rho}$, refer to Fig. 2) of the rigid airframe with the sensing orientation vector $\boldsymbol{s}$. The ideal specific force output of the accelerometer can be given by

$$A_n = \boldsymbol{s} \cdot \boldsymbol{f}_N. \tag{B-2}$$

Resolving the vectors in (B-1) and (B-2) into body frame, we have the following equations,

$$\begin{cases} f_b = [f_x, f_y, f_z]^T_{Body} \\ \alpha_b = [\alpha_x, \alpha_y, \alpha_z]^T_{Body} \\ \rho = [\rho_x, \rho_y, \rho_z]^T_{Body} \\ \omega_b = [\omega_x, \omega_y, \omega_z]^T_{Body} \\ s = [s_x, s_y, s_z]^T_{Body} \end{cases}$$

Thus (B-2) can be rewritten in a scalar form:

$$A_n = \begin{bmatrix} s_x \\ s_y \\ s_z \\ s_z\rho_y - s_y\rho_z \\ s_x\rho_z - s_z\rho_x \\ s_y\rho_x - s_x\rho_y \\ -s_y\rho_y - s_z\rho_z \\ -s_x\rho_x - s_z\rho_z \\ -s_x\rho_x - s_y\rho_y \\ s_x\rho_y + s_y\rho_x \\ S_x\rho_z + S_z\rho_x \\ s_y\rho_z + s_z\rho_y \end{bmatrix}^T_{Body} \begin{bmatrix} f_x \\ f_y \\ f_z \\ \alpha_x \\ \alpha_y \\ \alpha_z \\ \omega_x^2 \\ \omega_y^2 \\ \omega_z^2 \\ \omega_x\omega_y \\ \omega_x\omega_z \\ \omega_y\omega_z \end{bmatrix}_{Body} \tag{B-3}$$

Similarly, the ideal measurement of a gyroscope can be given by

$$G_n = \boldsymbol{s} \cdot \boldsymbol{\omega}_b = [s_x, s_y, s_z]_{Body} \begin{bmatrix} \omega_x \\ \omega_y \\ \omega_z \end{bmatrix}_{Body} \tag{B-4}$$

The measurement errors of MEMS IMU are usually modeled as misalignment error, scale factor error, bias and random noise. To focus on the core problem, only additive white Gaussian noise is considered after calibration. Hence, the measurements of IMU$_i$ ($i = 0, 1, 2, 3$) can be expressed as

$$\text{IMU}_i : \begin{cases} A_{ix} = A_{ix,n} + \xi_{ix} \\ A_{iy} = A_{iy,n} + \xi_{iy} \\ A_{iz} = A_{iz,n} + \xi_{iz} \\ G_{ix} = G_{ix,n} + \zeta_{ix} \\ G_{iy} = G_{iy,n} + \zeta_{iy} \\ G_{iz} = G_{iz,n} + \zeta_{iz} \end{cases} \tag{B-5}$$

where, ξ and ζ are noise. Because the 4 IMUs are installed parallel to the airframe body axes, the 24 measurement functions of the IMUs are easily obtained by combining Table. 2. It is easy to verify that IMU$_0$ has the simplest form as follows,

$$\text{IMU}_0 : \begin{cases} A_{0x} = f_x + \xi_{0x} \\ A_{0y} = f_y + \xi_{0y} \\ A_{0z} = f_z + \xi_{0z} \\ G_{0x} = \omega_x + \zeta_{0x} \\ G_{0y} = \omega_y + \zeta_{0y} \\ G_{0z} = \omega_z + \zeta_{0z} \end{cases} \tag{B-6}$$

Nevertheless, IMU_1 - IMU_3 have more complicated expressions, for example, IMU_1 with $\boldsymbol{\rho_1} = [-0.1, -0.5, 0]^T$

$$\mathrm{IMU}_1 : \begin{cases} A_{1x} = f_x + 0.5\alpha_z + 0.1\omega_y^2 + 0.1\omega_z^2 \\ \qquad -0.5\omega_x\omega_y + \xi_{1x} \\ A_{1y} = f_y - 0.1\alpha_z + 0.5\omega_x^2 + 0.5\omega_z^2 \\ \qquad -0.1\omega_x\omega_y + \xi_{1y} \\ A_{1z} = f_z - 0.5\alpha_x + 0.1\alpha_y - 0.1\omega_x\omega_y \\ \qquad -0.5\omega_y\omega_z + \xi_{1z} \\ G_{1x} = \omega_x + \zeta_{1x} \\ G_{1y} = \omega_y + \zeta_{1y} \\ G_{1z} = \omega_z + \zeta_{1z} \end{cases} \quad \text{(B-7)}$$

APPENDIX C
DISTURBANCE OBSERVER

The attitude dynamics (2) can be transformed into a cascaded form [32]–[34]

$$(\boldsymbol{E}^T\boldsymbol{I}\boldsymbol{E})\ddot{\boldsymbol{\xi}} = -(\boldsymbol{E}^T\boldsymbol{I}\dot{\boldsymbol{E}} + \boldsymbol{E}^T\boldsymbol{\Omega}\boldsymbol{I}\boldsymbol{E})\dot{\boldsymbol{\xi}} + \boldsymbol{E}^T\boldsymbol{M} + \boldsymbol{E}^T\boldsymbol{T} \quad \text{(C-1)}$$

where, $\boldsymbol{E} = \boldsymbol{Q}^{-1}$, $\boldsymbol{\xi} = [\phi, \theta, \psi]^T$ are Euler angles, and $\boldsymbol{\Omega}$ is skew-symmetric matrix form of $\boldsymbol{\omega}$. A simplified expression of (C-1) is given below,

$$\boldsymbol{J}\ddot{\boldsymbol{\xi}} = -\boldsymbol{C}\dot{\boldsymbol{\xi}} + \boldsymbol{\tau}_1 + \boldsymbol{d}_1. \quad \text{(C-2)}$$

A widely used nonlinear disturbance observer (NDO) from [30] can be given by

$$\begin{aligned} \dot{z} &= -\boldsymbol{K}\boldsymbol{J}^{-1}z + \boldsymbol{K}\boldsymbol{J}^{-1}(\boldsymbol{C}\dot{\boldsymbol{\xi}} - \boldsymbol{\tau}_1 - \boldsymbol{K}\dot{\boldsymbol{\xi}}), \\ \hat{\boldsymbol{d}}_1 &= z + \boldsymbol{K}\dot{\boldsymbol{\xi}}, \end{aligned} \quad \text{(C-3)}$$

where, $\boldsymbol{K}$ is the observer gain, $\hat{\boldsymbol{d}}_1$ is the disturbance estimation. The estimation of disturbance in body frame $\hat{\boldsymbol{T}}$ is $\boldsymbol{Q}^T\hat{\boldsymbol{d}}_1$. Note that, the NDO is based on an assumption that disturbances $\boldsymbol{d}_1$ are slowly time-varying, that is, $\dot{\boldsymbol{d}}_1 \approx 0$.

For (C-2), the input control torque $\boldsymbol{\tau}_1$ can be given by

$$\boldsymbol{\tau}_1 = \boldsymbol{u}_f + \boldsymbol{u}_c \quad \text{(C-4)}$$

where, $\boldsymbol{u}_f$ and $\boldsymbol{u}_c$ are the feedback and compensate actions, respectively. The term $\boldsymbol{u}_c$ can be chosen as $-\hat{\boldsymbol{d}}_1$ to compensate the disturbance. A robust control (RC) term $\boldsymbol{u}_f$ can be designed as [30], [38],

$$\boldsymbol{u}_f = \boldsymbol{J}\ddot{\boldsymbol{\xi}}_d + \boldsymbol{C}\dot{\boldsymbol{\xi}} - (\lambda_1 + \lambda_2\boldsymbol{J})\dot{\boldsymbol{\xi}}_e - \lambda_1\lambda_2\boldsymbol{\xi}_e \quad \text{(C-5)}$$

where, λ_1 and λ_2 are control gains. $\boldsymbol{\xi}_d$ are desired Euler angles and $\boldsymbol{\xi}_e$ are the Euler angle errors defined as $\boldsymbol{\xi}_e = \boldsymbol{\xi} - \boldsymbol{\xi}_d$. The closed loop stability can refer to [30].

ACKNOWLEDGMENT

Z. Ren thanks Prof. Kai Chen for his kind help on MEMS IMU.

REFERENCES

[1] M. Mazur, A. Wisniewski, and J. McMillan, *Clarity from Above: PWC Global Report on the Commercial Applications of Drone Technology*. London, U.K.: PriceWater house Coopers, 2016.
[2] H. Shakhatreh, A. H. Sawalmeh, A. Al-Fuqaha, Z. Dou, E. Almaita, I. Khalil, N. S. Othman, A. Khreishah, and M. Guizani, "Unmanned aerial vehicles (UAVs): A survey on civil applications and key research challenges," *IEEE Access*, vol. 7, pp. 48572–48634, 2019.
[3] K. Maeda, S. Doki, Y. Funabora, and K. Doki, "Flight path planning of multiple UAVs for robust localization near infrastructure facilities," in *Proc. 44th Annu. Conf. IEEE Ind. Electron. Soc.*, Oct. 2018, pp. 2522–2527.
[4] O. Anicho, P. B. Charlesworth, G. Baicher, and A. Nagar, "Integrating routing schemes and platform autonomy algorithms for UAV Ad-hoc & infrastructure based networks," in *Proc. 28th Int. Telecommun. Netw. Appl. Conf. (ITNAC)*, Nov. 2018, pp. 1–5.
[5] M. Buchaillot, A. Gracia-Romero, O. Vergara-Diaz, M. A. Zaman-Allah, A. Tarekegne, J. E. Cairns, B. M. Prasanna, J. L. Araus, and S. C. Kefauver, "Evaluating maize genotype performance under low nitrogen conditions using RGB UAV phenotyping techniques," *Sensors*, vol. 19, no. 8, p. 1815, Jan. 2019.
[6] Z. Hu, Z. Bai, Y. Yang, Z. Zheng, K. Bian, and L. Song, "UAV aided aerial-ground IoT for air quality sensing in smart city: Architecture, technologies, and implementation," *IEEE Netw.*, vol. 33, no. 2, pp. 14–22, Apr. 2019.
[7] Y. Yu, Z. Li, X. Liu, K. Hirota, X. Chen, T. Fernando, and H. H.-C. Iu, "A nested tensor product model transformation," *IEEE Trans. Fuzzy Syst.*, vol. 27, no. 1, pp. 1–15, Jan. 2019.
[8] K. Kuru, D. Ansell, W. Khan, and H. Yetgin, "Analysis and optimization of unmanned aerial vehicle swarms in logistics: An intelligent delivery platform," *IEEE Access*, vol. 7, pp. 15804–15831, 2019.
[9] J. A. Shaffer, E. Carrillo, and H. Xu, "Hierarchal application of receding horizon synthesis and dynamic allocation for uavs fighting fires," *IEEE Access*, vol. 6, pp. 78868–78880, 2018.
[10] C. Cheung and B. Grocholsky, "UAV-UGV collaboration with a PackBot UGV and Raven SUAV for pursuit and tracking of a dynamic target," *Proc. SPIE*, vol. 6962, Apr. 2008, Art. no. 696216.
[11] P. Merritt, J. Donaldson, D. O'Brien, K. Coleman, and G. Pyles, "Angular vibration survey of various aircraft," *Proc. SPIE*, vol. 5087, Aug. 2003, pp. 35–45.
[12] A. Mohamed, K. Massey, S. Watkins, and R. Clothier, "The attitude control of fixed-wing MAVS in turbulent environments," *Progr. Aerosp. Sci.*, vol. 66, pp. 37–48, Apr. 2014.
[13] X. Liu, L. Li, Z. Li, X. Chen, T. Fernando, H. H. Iu, and G. He, "Event-trigger particle filter for smart grids with limited communication bandwidth infrastructure," *IEEE Trans. Smart Grid*, vol. 9, no. 6, pp. 6918–6928, Nov. 2018.
[14] D. R. Nelson, D. B. Barber, T. W. McLain, and R. W. Beard, "Vector field path following for small unmanned air vehicles," in *Proc. Amer. Control Conf.*, 2006, pp. 1–7.
[15] S. Watkins, J. Milbank, B. J. Loxton, and W. H. Melbourne, "Atmospheric winds and their implications for microair vehicles," *AIAA J.*, vol. 44, no. 11, pp. 2591–2600, Nov. 2006.
[16] A. Mohamed, S. Watkins, R. Clothier, M. Abdulrahim, K. Massey, and R. Sabatini, "Fixed-wing MAV attitude stability in atmospheric turbulence, part 1: Suitability of conventional sensors," *Progr. Aerosp. Sci.*, vol. 70, pp. 69–82, Oct. 2014.
[17] P. Schopp, L. Klingbeil, C. Peters, and Y. Manoli, "Design, geometry evaluation, and calibration of a gyroscope-free inertial measurement unit," *Sens. Actuators A, Phys.*, vol. 162, no. 2, pp. 379–387, Aug. 2010.
[18] G. M. Gremillion and J. S. Humbert, "Disturbance rejection with distributed acceleration sensing for small unmanned aircraft systems," *AIAA J.*, vol. 13, pp. 2233–2246, May 2016.
[19] X. Shao, J. Liu, and H. Wang, "Robust back-stepping output feedback trajectory tracking for quadrotors via extended state observer and sigmoid tracking differentiator," *Mech. Syst. Signal Proc.*, vol. 104, pp. 631–647, Mar. 2018.
[20] R. C. Nelson, *Flight Stability and Automatic Control*, vol. 2. New York, Ny, USA: McGraw Hill, 1998.
[21] A. Dorobantu, A. Murch, B. Mettler, and G. Balas, "System identification for small, low-cost, fixed-wing unmanned aircraft," *J. Aircr.*, vol. 50, no. 4, pp. 1117–1130, Jul. 2013.
[22] InvenSense. (2018). *Mpu-6050|Tdk*. [Online]. Available: https://www.invensense.com/products/motion-tracking/6-axis/mpu-6050/

[23] M. Jafari, "Optimal redundant sensor configuration for accuracy increasing in space inertial navigation system," *Aerosp. Sci. Technol.*, vol. 47, pp. 467–472, Dec. 2015.
[24] S. Li, L. Li, Z. Li, X. Chen, T. Fernando, H. H. Iu, G. He, Q. Wang, and X. Liu, "Event-trigger heterogeneous nonlinear filter for wide-area measurement systems in power grid," *IEEE Trans. Smart Grid*, vol. 10, no. 3, pp. 2752–2764, May 2019.
[25] R. Tedrake. (Feb. 1, 2019). Underactuated robotics: Algorithms for walking, running, swimming, flying, and manipulation [Course Notes for MIT 6.832]. [Online]. Available: http://underactuated.mit.edu/
[26] B. Dai, Y. He, G. Zhang, F. Gu, L. Yang, and W. Xu, "Wind disturbance rejection for unmanned aerial vehicle based on acceleration feedback method," in *Proc. IEEE Conf. Decision Control (CDC)*, Dec. 2018, pp. 4680–4686.
[27] Y. C. Paw, "Synthesis and validation of flight control for UAV," Ph.D. Dissertation, University of Minnesota, Minneapolis, MN, USA, 2009.
[28] B. L. Stevens and F. L. Lewis, *Aircraft Control Simulation*. Hoboken, NJ, USA: Wiley, 1992.
[29] Z. Ren, W. Fu, J. Yan, and B. Xu, "Discrete reconfigurable back-stepping attitude control of reentry hypersonic flight vehicle," *Adv. Mech. Eng.*, vol. 9, no. 4, pp. 1–10, Apr. 2017.
[30] S. Li, J. Yang, W.-H. Chen, and X. Chen, *Disturbance Observer-Based Control : Methods Application*. Boca Raton, FL, USA: CRC Press, 2016.
[31] B. Liu, Z. Li, X. Chen, Y. Huang, and X. Liu, "Recognition and vulnerability analysis of key nodes in power grid based on complex network centrality," *IEEE Trans. Circuits Syst., II, Exp. Briefs*, vol. 65, no. 3, pp. 346–350, Mar. 2018.
[32] X. Shao, J. Liu, H. Cao, C. Shen, and H. Wang, "Robust dynamic surface trajectory tracking control for a quadrotor UAV via extended state observer," *Int. J. Robust Nonlinear Control*, vol. 28, no. 7, pp. 2700–2719, 2018.
[33] X. Shao, L. Wang, J. Li, and J. Liu, "High-order ESO based output feedback dynamic surface control for quadrotors under position constraints and uncertainties," *Aerosp. Sci. Technol.*, vol. 89, pp. 288–298, Jun. 2019.
[34] M. R. Mokhtari, A. C. Braham, and B. Cherki, "Extended state observer based control for coaxial-rotor UAV," *ISA Trans.*, vol. 61, pp. 1–14, Mar. 2016.
[35] M. R. Mokhtari, B. Cherki, and A. C. Braham, "Disturbance observer based hierarchical control of coaxial-rotor UAV," *ISA Trans.*, vol. 67, pp. 466–475, Mar. 2017.
[36] Z. Ren, W. Fu, S. Zhu, B. Yan, and J. Yan, "Bio-inspired neural adaptive control of a small unmanned aerial vehicle based on airflow sensors," *Sensors*, vol. 18, no. 10, p. 3233, 2018.
[37] K. Reif, S. Günther, E. Yaz, and R. Unbehauen, "Stochastic stability of the discrete-time extended Kalman filter," *IEEE Trans. Autom. Control*, vol. 44, no. 4, pp. 714–728, Apr. 1999.
[38] J. Liu, *Sliding Mode Control Design MATLAB Simulation: Design Method Advertisment Control System*. Beijing, China: Tsinghua Univ. Press, 2015.

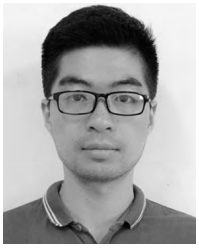

ZIJUN REN received the M.S. degree in aerospace engineering from Northwestern Polytechnical University, in 2015, where he is currently pursuing the Ph.D. degree. His research interests include UAV flight control, system simulation, fault diagnosis, and control theory.

WENXING FU was born in Xi'an, China, in 1974. He received the Ph.D. degree in aerospace engineering from the School of Astronautics, Northwestern Polytechnical University, in 2006. He visited Cranfield University, England, from 2012 to 2013. He has published several books. He is currently a Professor of aerospace engineering with Northwestern Polytechnical University and the Co-Director of the Flight Control and Simulation Laboratory. His research interests include the system simulation, aircraft design, guidance, and control of flight vehicles.

YONGZE LI received the M.S. degree from Northwestern Polytechnical University, in 2012. He is currently an Engineer with the Institute of Systems Engineering, China Academy of Engineering Physics, Mianyang, China. His research interest includes the design of UAVs.

BINBIN YAN received the Ph.D. degree in aerospace engineering from the School of Astronautics, Northwestern Polytechnical University, in 2010, where he is currently an Associate Professor of aerospace engineering. His research interests include the aircraft control, guidance, and simulation.

SUPENG ZHU received the Ph.D. degree from the School of Astronautics, Northwestern Polytechnical University, in 2011. She is currently an Associate Professor with the School of Astronautics. Her current research interests include intelligent control and simulation.

JIE YAN received the Ph.D. degree from the School of Astronautics, Northwestern Polytechnical University, in 1988.

He is currently a Senior Professor with the School of Astronautics, Northwestern Polytechnical University. His research interests include flight control, guidance, system simulation, and aircraft design.